

Optical saturation effects in intracavity Faraday modulation spectroscopy (INFAMOS)

Cite as: J. Chem. Phys. **149**, 174202 (2018); <https://doi.org/10.1063/1.5040577>

Submitted: 18 May 2018 . Accepted: 19 October 2018 . Published Online: 06 November 2018

Tomás H. P. Pinto , Michele Gianella , and Grant A. D. Ritchie 



View Online



Export Citation



CrossMark

ARTICLES YOU MAY BE INTERESTED IN

[A magnetic guide to purify radical beams](#)

The Journal of Chemical Physics **149**, 174201 (2018); <https://doi.org/10.1063/1.5053656>

[Communication: Substantial impact of the orientation of transition dipole moments on the dynamics of diatomics in laser fields](#)

The Journal of Chemical Physics **149**, 181101 (2018); <https://doi.org/10.1063/1.5054775>

[Dynamics of polar polarizable rotors acted upon by unipolar electromagnetic pulses: From the sudden to the adiabatic regime](#)

The Journal of Chemical Physics **149**, 174109 (2018); <https://doi.org/10.1063/1.5051591>

Lock-in Amplifiers
... and more, from DC to 600 MHz



Optical saturation effects in intracavity Faraday modulation spectroscopy (INFAMOS)

Tomás H. P. Pinto, Michele Gianella, and Grant A. D. Ritchie^{a)}

Department of Chemistry, Physical and Theoretical Chemistry Laboratory, University of Oxford, South Parks Road, Oxford OX1 3QZ, United Kingdom

(Received 18 May 2018; accepted 19 October 2018; published online 6 November 2018)

We report on the observation of saturation effects in Intracavity Faraday Modulation Spectroscopy (INFAMOS). A quantum cascade laser operating at $\sim 5.3 \mu\text{m}$ is used to probe the $^2\Pi_{3/2}$ and $^2\Pi_{1/2}$ R(3,5) transitions in the fundamental band of nitric oxide. With average intracavity intensities up to 450 W cm^{-2} , the saturation of these molecular transitions is observed up to a total pressure of ~ 240 Torr. The experimental data are interpreted by incorporating saturation into a model for the INFAMOS line shape in the homogeneously broadened limit. *Published by AIP Publishing.*
<https://doi.org/10.1063/1.5040577>

I. INTRODUCTION

Saturation spectroscopy encompasses a variety of laser based techniques most commonly aimed at removing Doppler broadening and probing molecular hyperfine structures of low pressure gas samples.^{1–3} These include Lamb-dip and polarisation spectroscopies, which also find applications in laser frequency stabilization,^{4–7} linewidth measurements,^{8,9} in plasma diagnostics for determining electric field strengths from Stark splitting,¹⁰ and in the measurement of transition dipole moments.³ While saturation often relies upon intense (saturating) radiation, which was initially provided by high power lasers, it can also be achieved with lower power continuous wave (cw) diode lasers by probing atomic transitions whose absorption cross sections are several orders of magnitude larger than molecular cross sections.^{11–13} However, by using resonant optical cavities, it is possible to saturate molecular transitions with weak cw diode sources. For example, Lisak and Hodges have used a cavity ring-down spectroscopy (CRDS) configuration to obtain accurate frequency markers from Lamb-dips in H_2O spectra with a diode laser with an optical power output of 5 mW, operated at $\sim 1.4 \mu\text{m}$.¹⁴

Saturation effects have found an application in cavity based methods with Giusfredi *et al.* developing saturated cavity ring-down spectroscopy (SCAR), a technique that improves the sensitivity of conventional CRDS by decoupling absorber related losses from empty-cavity ring-down time variations in a single ring-down event.¹⁵ In his original work, SCAR was demonstrated with the measurement of the hyperfine structure of a transition from a vibrationally excited state of $^{17}\text{O}^{12}\text{C}^{16}\text{O}$ using a mid-IR difference frequency-generated cw source. An extension of the technique to quantum cascade lasers (QCLs) was later demonstrated in the work by Galli *et al.*, where a SCAR based spectrometer was used

for the detection of radiocarbon dioxide down to a parts-per-quadrillion level.¹⁶ In a recent report, Ventrillard *et al.* have presented evidence of saturation of NO transitions probed with a QCL based optical-feedback cavity enhanced absorption spectroscopy (OF-CEAS) apparatus, where the large intracavity power offered by optical feedback locking caused the underestimation of the absorption coefficient at the line centre by 40% at a total pressure of 76 Torr.¹⁷ Saturation has also been studied theoretically and experimentally in noise-immune cavity-enhanced optical heterodyne molecular spectroscopy (NICE-OHMS) in the near-IR by Axner *et al.*^{18–20} Interestingly, these studies were conducted in the Doppler- and sub-Doppler-broadened regimes and showed that while the absorptive component of the measured signal exhibits a reduction in amplitude at all pressures caused by the large intracavity irradiance, the dispersive component remains virtually unaffected in the low pressure (Doppler-broadened) limit.

Recently, we have reported on Intracavity Faraday Modulation Spectroscopy (INFAMOS), a technique that combines the sensitivity (and high intracavity power) of an OF-CEAS system with the selectivity of a Faraday modulation spectrometer (FAMOS).²¹ FAMOS is a well established technique for the detection of paramagnetic species (or radicals), such as NO, OH, O_2 , and HO_2 , which are of great importance in atmospheric chemistry and medicine. Additionally, FAMOS offers reasonable immunity to common interferent species, such as CO_2 and water.^{22–24} The technique is based on the net rotation of the plane of polarization of linearly polarized light as it propagates through a paramagnetic sample that is made birefringent by the application of a longitudinal magnetic field. The coupling of Faraday modulation spectrometers with high finesse optical cavities has been recently demonstrated in the near-IR with the detection of molecular oxygen by Westberg *et al.* using a cavity ring-down configuration in a DC magnetic field²⁵ and in the mid-IR using INFAMOS (in an AC field) for the detection of NO by Gianella *et al.*, with the same spectrometer used in this work. INFAMOS requires a stable cavity

^{a)}Electronic mail: grant.ritchie@chem.ox.ac.uk

throughput for a time period long enough for the lock-in amplifier to demodulate the signal, and optical-feedback locking is an ideal candidate for this purpose.^{26–29} When on resonance with a longitudinal mode of an external optical cavity, the laser can be frequency locked to the returning resonant wave if its phase matches that of the wave emitted at the laser facet. This induces a linewidth narrowing such that the “locked” laser bandwidth is reduced to the bandwidth of the optical cavity itself, resulting in more efficient coupling and circulating powers of the order of Watts with mid-IR QCLs, sufficient to saturate molecular transitions.

In our previous work, we observed discrepancies between the measured and theoretical INFAMOS spectra which were attributed to optical saturation.²¹ Similar effects have been previously observed in single-pass Faraday rotation experiments involving DC magnetic fields in noble gas discharges and in atomic vapours between pressures of 1 and 10 Torr, using a diode laser and a dye laser, respectively, with intensities up to 1 W cm^{-2} .^{30,31} In this paper, we present a more detailed description of saturation effects in INFAMOS when probing the $^2\Pi_{3/2}$ and $^2\Pi_{1/2}$ R(3.5) transitions of NO, using the simultaneously generated OF-CEAS spectra as a support. In addition to this, a model for saturated INFAMOS is presented and compared to experimental observations. Saturation is an increasingly prevalent phenomenon in resonant cavity based techniques in the mid-IR due to the emergence of QCLs, which can provide output powers of a few hundreds of mW in cw operation in a region of strong molecular absorption, and so a better understanding of the impact that this will have on modern spectroscopic techniques is required.

The structure of the paper is as follows: Secs. II and III provide a brief overview of Faraday rotation and saturation and also introduce the key equations used in our simulations and in presenting the INFAMOS spectrometer. In Sec. IV, the effects of saturation are demonstrated using the spectra obtained at pressures ranging from 39 Torr to 240 Torr, with a spectrometer based on a QCL emitting at $\sim 5.3 \mu\text{m}$ providing peak intensities up to 1.4 kW cm^{-2} in a 78 cm long linear cavity with magnetic fields strengths between 50 G and 100 G. The paper then concludes with a comparison between saturated INFAMOS spectra and a simulation produced using the model detailed in Sec. II.

II. THEORETICAL OVERVIEW

A. Intracavity Faraday modulation spectroscopy: INFAMOS

The Faraday effect is at the core of Faraday modulation spectroscopy (FAMOS) and is defined as the rotation of the plane of polarization of linearly polarized light as it traverses a paramagnetic sample that is subject to a longitudinal magnetic field. This field lifts the degeneracy of the energy levels with the magnetic quantum number M , associated with a rotational state with the total angular momentum quantum number J and multiplicity $2J + 1$. A linearly polarized electromagnetic wave can be treated as the combination of two circularly polarized components, left-hand circularly

polarized (LHCP) and right-hand circularly polarized (RHCP), each of which interacts independently with a subset of $\Delta M = +1$ and $\Delta M = -1$ transitions, respectively. Moreover, as the two circularly polarized waves experience different attenuation and phase shift as they propagate through the sample, the medium presents both magnetic circular dichroism (MCD) and magnetic circular birefringence (MCB). The Faraday rotation angle, θ , is obtained from the phase difference (MCB) between the LHCP and RHCP, ϕ^L and ϕ^R , components of the wave

$$\theta = \frac{\phi^L - \phi^R}{2}. \quad (1)$$

An identical relation between the attenuation experienced by the two polarizations would yield dichroism, \mathcal{D} , as it is related to birefringence via the Kramers-Kronig relations.³²

In the unsaturated case, the phase-shift experienced by circularly polarized monochromatic light with frequency ν can be modelled as [Appendix E, Eq. (E3)]

$$\phi_q(\nu) = \text{const} + \frac{\mathcal{N}\mathcal{F}L}{2} \mathcal{M}'_q(\nu), \quad (2)$$

where \mathcal{N} is the molecular number density, \mathcal{F} is the line strength of the transition, L is the light-sample interaction length, $q = +1$ for LHCP, $q = -1$ for RHCP, and \mathcal{M}'_q is the dispersive line shape given by [Appendix B, Eq. (B8)]

$$\mathcal{M}'_q(\nu) = 3 \sum_{M,M'} \begin{pmatrix} J' & 1 & J \\ -M' & q & M \end{pmatrix}^2 \chi(\nu; \nu_0^{MM'}), \quad (3)$$

where χ [Appendix A, Eq. (A15)] is the dispersive line shape for a single $|J, M\rangle \rightarrow |J', M'\rangle$ transition centred at the Zeeman-shifted transition centre [Appendix A, Eq. (A20)]

$$\nu_0^{MM'} = \nu_0 + (g'M' - gM) \frac{\mu_B B}{hc}. \quad (4)$$

In Eq. (4), ν_0 is the transition centre in the zero-field case, g and g' are the g -factors of the lower and upper states, respectively, and B is the magnetic field strength.

The Faraday rotation angle that results from these two independent phase shifts is then also a function of magnetic field and interaction distance within a paramagnetic sample. The effective path length increases substantially by coupling a FAMOS spectrometer with an optical cavity, resulting in a Faraday rotation angle magnified by the finesse \mathcal{F} of the cavity³³

$$\theta_{\text{cav}} = \frac{2\mathcal{F}}{\pi} \theta, \quad (5)$$

where, for a linear cavity, the finesse is given by $\mathcal{F} \approx \pi\sqrt{R(1-R)^{-1}}$ with average mirror reflectivity R . This translates into a Faraday rotation angle enhancement factor, provided by our mirrors with $R = 0.9998$, of $\approx 1 \times 10^4$.

Trace gas detection using the Faraday effect can employ both static and modulated magnetic fields, with the latter providing the benefit of detection at higher frequencies and hence the rejection of low frequency noise. This modulation scheme is similar to the one in wavelength modulation spectroscopy (WMS)³⁴ but instead relies on the modulation of the optical transitions as opposed to the laser frequency. The intensity of the Faraday modulation signal measured at the first harmonic by a lock-in amplifier is proportional to the first Fourier

coefficient of the Fourier representation of the now time dependent and periodic birefringence and dichroism. The full details of the theory surrounding the base INFAMOS model is covered in our previous work²¹ and in the work by other authors.³⁵

B. Saturation of optical transitions

In the presence of a magnetic field, the (unsaturated) absorption of a circularly polarized wave ($q = +1$: LHCP, $q = -1$: RHCP) at the frequency ν , $\alpha_q(\nu)$, for a transition $|J\rangle \rightarrow |J'\rangle$ consists of the sum of the contributions from all allowed sub-transitions $|J, M\rangle \rightarrow |J', M'\rangle$

$$\alpha_q(\nu) = \mathcal{N}\mathcal{S}\mathcal{M}_q(\nu), \quad (6)$$

where \mathcal{N} is the molecular number density, \mathcal{S} is the line strength, and \mathcal{M}_q is the absorptive line shape function, given by

$$\mathcal{M}_q(\nu) = 3 \sum_{M, M'} \begin{pmatrix} J' & 1 & J \\ -M' & q & M \end{pmatrix}^2 \eta(\nu; \nu_0^{MM'}), \quad (7)$$

where η [Appendix A, Eq. (A16)] is the absorptive line shape function for a single $|J, M\rangle \rightarrow |J', M'\rangle$ transition centred at $\nu_0^{MM'}$. The energy separation between $|J, M\rangle$ and $|J, M+1\rangle$ for $B = 100$ G is simply $g\mu_B B/(hc)$ and takes values in the range 0.0001 cm^{-1} – 0.001 cm^{-1} for g values between 0.02 and 0.2. Doppler (FWHM = 0.00425 cm^{-1}) and pressure broadening contributions are significantly larger, and therefore there is a strong overlap between the line shapes of each sub-transition, η , so that any given laser frequency ν will probe virtually all sub-transitions simultaneously. Clearly, if the intensity is large enough, the populations of *all* the upper and lower states change due to optical pumping.

To begin with, we assume that the pressure is large enough that no spectral hole burning occurs, i.e., the number of molecules in a given state and with a velocity component v along the axis of propagation of a light wave is given by the Maxwell-Boltzmann distribution (homogeneous limit). This greatly simplifies the rate equations for the populations of the upper and lower states of the transition [Appendix D, Eq. (D1)]. There are then two extreme cases we can consider. In the first case, we assume no relaxation among the lower sub-states, $|J, M\rangle$, nor among the upper sub-states, $|J', M'\rangle$; the laser beam alters the population of the lower, N_{JM} , and upper, $N_{J'M'}$, states of each sub-transition independently. Each sub-transition then has its own population difference (and saturation parameter). The net (observed) line shape then consists of the weighted sum of all the individual line shapes, where the weights include not only the different transition moments of each sub-transition [given by the Wigner 3j symbols in the present case, see Eq. (B7)] but also the sub-transition-specific population difference. In the second case, we assume instantaneous relaxation among the lower sub-states and among the upper sub-states such that the population is distributed evenly across all the lower (upper) sub-states, $N_{JM} = N_J/g_J$ ($N_{J'M'} = N_{J'}/g_{J'}$). The net line shape is given by Eq. (B7) but scaled by a factor common to all sub-transitions, $p_q(\nu)$. This second case is the one used for our derivations

in Appendix B [see. Eq. (B5)]. The saturated absorption then becomes [Appendix E, Eq. (E2)]

$$\alpha_q = \mathcal{N}\mathcal{S}p_q(\nu)\mathcal{M}_q(\nu), \quad (8)$$

with the fractional population given by [Appendix D, Eq. (D9)]

$$p_q(\nu) = \frac{1}{1 + S_q(\nu)}, \quad (9)$$

and the saturation parameter [Appendix D, Eq. (D7)]

$$S_q(\nu) = \frac{I}{I_q^{\text{sat}}(\nu)} = \pi\gamma S_0\mathcal{M}_q(\nu), \quad (10)$$

where S_0 is the saturation parameter at the line centre.

Often, an alternative saturation intensity, I_0^{sat} , is defined as the irradiance required to halve the measured absorption at the centre of the transition in the zero-field, high-pressure limit. In this limit [Appendix D, Eq. (D12)]

$$I_0^{\text{sat}} \sim \frac{1}{\sigma_0\tau}, \quad (11)$$

where σ_0 is the absorption cross section at the transition centre and τ is the lifetime of the upper state. For NO ($v = 1$), the collisional vibrational relaxation rate constant is $\sim 4.5 \text{ s}^{-1} \text{ Torr}^{-1}$.³⁶ At 75 Torr, for example, this corresponds to an upper state lifetime of ~ 3 ms and should be regarded as an upper limit for the system's relaxation time, since the transit-time through a 1 mm diameter beam shortens the relaxation time to $\sim 2 \mu\text{s}$. Other contributions to upper state depopulation, such as rotational energy transfer, reduce the lifetime even further.

The significantly higher $v = 1 \leftarrow 0$ pumping rates that are attained with the optical feedback technique compared to non-resonant cavity based methods are a consequence of the large intra-cavity intensity built up due to the markedly increased coupling efficiency. The intensity of a TEM₀₀ cavity mode at any point along the cavity axis, $I_0(z)$, is given by

$$I_0(z) = \frac{2P_{\text{circ}}}{\pi w^2(z)}, \quad (12)$$

where w is the beam radius at a point along the z axis and P_{circ} , the circulating power, can be estimated with

$$P_{\text{circ}} = \frac{2P_{\text{out}}}{(1 - R)}. \quad (13)$$

Here, R is the cavity mirror reflectivity and P_{out} is the transmitted power. With mirror reflectivities up to 0.9998 and transmitted powers of 0.8 mW (measured with a calibrated power meter after the cavity), the maximum intensity at the centre of the spectrometer is $I_0(0) = 1.4 \text{ kW cm}^{-2}$. The intensity also depends on the radial coordinate, r , as

$$I(r, z) = I_0(z)e^{-2(\frac{r}{w})^2}. \quad (14)$$

The saturation observed in both INFAMOS and OF-CEAS signals is then a geometric average of the saturation observed at all points in the cavity, which varies according to the local intensity. Using Eqs. (12)–(14) and integrating over the intra-cavity volume which satisfies the condition $I(r, z) \geq I_0e^{-2}$, the average intensity I_{av} is estimated at 447 W cm^{-2} . Since higher

order cavity modes have larger radii and experience higher diffraction losses, this should be regarded as the upper limit of intracavity intensity.

The saturated refractive index and absorption coefficient for circular polarization q are [Appendix E, Eqs. (E1) and (E2)]

$$n_q(\nu) = 1 + \frac{1}{4\pi\nu} \frac{\mathcal{N}\mathcal{P}\mathcal{M}'_q(\nu)}{1 + \pi\gamma S_0\mathcal{M}_q(\nu)}, \quad (15)$$

$$\alpha_q(\nu) = \frac{\mathcal{N}\mathcal{P}\mathcal{M}_q(\nu)}{1 + \pi\gamma S_0\mathcal{M}_q(\nu)}. \quad (16)$$

The resulting phase-shift for polarization q is then [Appendix E, Eq. (E3)]

$$\phi_q(\nu) = \text{const} + \frac{\mathcal{N}\mathcal{P}\mathcal{L}}{2} \frac{\mathcal{M}'_q(\nu)}{1 + \pi\gamma S_0\mathcal{M}_q(\nu)}. \quad (17)$$

III. EXPERIMENTAL

Figure 1 shows a schematic representation of the INFAMOS spectrometer. A distributed feedback (DFB) QCL (Maxion M575AY) operating in continuous wave (cw) mode is the laser source. The laser emits up to 100 mW of optical power within a range of 1883–1894 cm^{-1} and is driven by a home-built driver. As a requirement for the operation of our linear optical-feedback cavity,³⁷ an iris, onto which the laser beam is focused by a parabolic mirror, is placed after an optical delay line with the aim of mitigating the effect of non-resonant optical feedback on the laser by spatially filtering a significant part of the unwanted returning wave. The piezo mounted mirror (MPZ) before the cavity is responsible for fine adjustment of the laser to cavity distance to ensure phase matching of the intracavity feedback field into the laser. After a mode-matching lens and a polariser, two highly reflective dielectric coated mirrors (Los Gatos Research, $R = 0.9998$) with a radius of curvature (ROC) of 0.5 m comprise the cavity, the optical axis of which coincides with the longitudinal axis of the solenoid. A beam splitter (Thorlabs BSW510) separates the cavity output

into two paths that are simultaneously collected by detectors D1 and D2. The first photodetector, D1 (Vigo System S.A. PVI-2TE-6/VPDC-20I), is placed after a polarization analyzer (LOT-QuantumDesign SIR3-5) at an uncrossing angle $\beta \approx 2^\circ$. The output of D1 is demodulated by a lock-in amplifier (Stanford Research Systems SR830) which in turn drives the solenoid with an amplified (QSC Audio RMX 4050 HD) 7.5 kHz sine wave. The second photodetector, D2 (Vigo System S.A. PVMI-3TE-10.6-MIPDC-F-20), monitors the cavity output simultaneously and produces the OF-CEAS spectrum. The intra-cavity power build-up, combined with the large absorption cross sections of the fundamental band of NO, is sufficient to induce saturation of the spectroscopic transitions which are shown and modelled in Sec. IV. Trace concentrations of NO are achieved by mixing a calibrated 15 ppmv NO in nitrogen gas mixture (BOC) with dry nitrogen (BOC). The two gas flows were controlled and regulated by two mass flow controllers (Tylan FC-260), combined and passed through the cavity. The total pressure is chosen by maintaining a constant gas inflow of NO and N_2 and restricting the outflow with a valve. The total pressure increases until these two flows equilibrate. The oscillating magnetic field applied longitudinally to the optical cavity is generated by a water cooled solenoid capable of producing magnetic fields with amplitudes up to 240 G at 7.5 kHz.²¹

IV. RESULTS AND DISCUSSION

The INFAMOS spectrometer produces two simultaneous outputs, the raw cavity transmission and the Faraday rotation signal (lock-in amplifier output). From the former, OF-CEAS spectra can be constructed, and these provide a useful tool for establishing the intensity conditions within the optical cavity. An example transmission spectrum is shown in Fig. 2 with the maxima appearing at the times during the scan that the laser is on resonance with a longitudinal mode of the cavity. With a 78 cm long linear cavity, these maxima are separated in

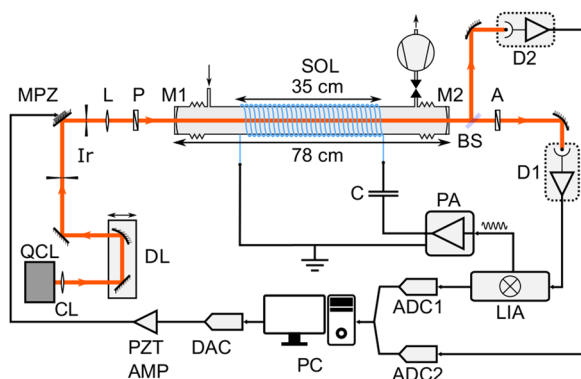


FIG. 1. Schematic of the INFAMOS spectrometer (adapted from Ref. 21). QCL: quantum cascade laser; L: collimating lens; DL: optical delay line; Ir: iris; MPZ: piezo mounted mirror; PZT AMP: piezo amplifier; MM: mode matching lens; P: polarizer; M1 and M2: cavity mirrors 1 and 2; SOL: solenoid; BS: beam splitter; A: analyzer; D1 and D2: detectors 1 and 2; LIA: lock-in amplifier; PA: audio amplifier; ADC1 and 2: analog to digital converter 1 and 2; DAC: digital to analog converter.

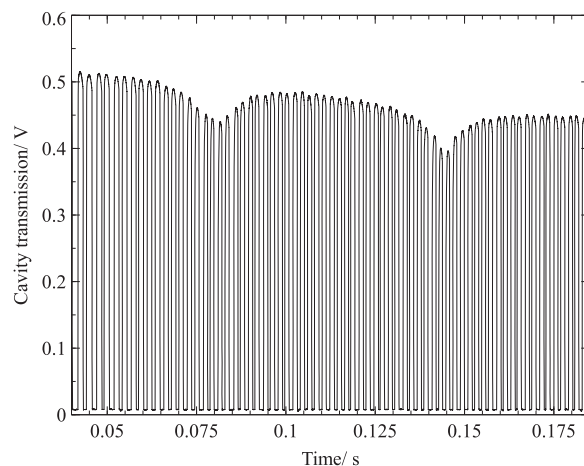


FIG. 2. Raw cavity transmission on a frequency up-sweep, monitored during the acquisition of an INFAMOS spectrum. The raw cavity transmission in a single sweep across the $^2\Pi_{3/2}$ and $^2\Pi_{1/2}$ R(7/2) transitions of NO, at a repetition rate of 5 Hz, a total pressure of 50 Torr, and a mixing ratio of 0.22 ppmv in dry nitrogen.

frequency by the free spectral range $\text{FSR} = 192 \text{ MHz}$. Taking the amplitude at each point, OF-CEAS spectra such as those shown in Fig. 3 can be constructed since the absorption coefficient, α , can be related to the cavity transmission with³⁷

$$\alpha = \frac{(1-R)}{L} \left[\sqrt{\frac{T_0}{T}} - 1 \right], \quad (18)$$

where T and T_0 are the transmission with and without the presence of an absorber, respectively. Since the length L is known, the *apparent* mirror reflectivity can be inferred (see below) from an unsaturated absorption of a sample of known concentration.

Figure 3 shows the measured absorption coefficient, $\alpha(\nu)$, obtained for two samples of NO at total pressures of 39 and 75 Torr and a mixing ratio of 940 ppbv in N_2 . Under these conditions, the Lorentzian widths calculated using the HITRAN pressure broadening parameters are 187 MHz and 360 MHz, respectively. However, fitting these spectra with a Voigt profile with a fixed FWHM Gaussian component of 126 MHz (the Doppler width of NO at 298 K) yields Lorentzian components (FWHM) of $471 \pm 22 \text{ MHz}$ and $567 \pm 15 \text{ MHz}$ at 39 Torr and 75 Torr, respectively. This marked increase in linewidth is a signature of optical saturation. In addition, it can be seen that the absorption at the line centre is at least a factor of 2 smaller than expected. A saturation parameter at the line centre calculated via the homogeneous width of the transitions, $S_{0,\gamma}$, can then be extracted using the relationship³⁸

$$\gamma_S = \gamma_0 \sqrt{1 + S_{0,\gamma}}, \quad (19)$$

where γ_S is the saturated homogeneous width and γ_0 is the unsaturated homogeneous width. Applying this treatment to the spectra obtained at 39 Torr and 75 Torr yields $S_{0,\gamma} = 5.3$ and $S_{0,\gamma} = 1.5$, respectively. A similar procedure can be followed for calculating the saturation parameter at the line centre using

the absorption coefficients, $S_{0,\alpha}$, via

$$\alpha_S = \frac{\alpha_0}{1 + S_{0,\alpha}}. \quad (20)$$

The saturation parameters extracted this way from the spectra recorded at 39 Torr and 79 Torr are $S_{0,\alpha} = 3.5$ and $S_{0,\alpha} = 1.3$, respectively. We note that it is common for the parameters $S_{0,\gamma}$ and $S_{0,\alpha}$ to have different values, as α is affected by saturation in both the homogeneous and inhomogeneous broadening limits whereas γ is only dependent on homogeneous broadening mechanisms.³⁸ The comparison between these parameters as a function of pressure is shown in Fig. 4, and as expected, saturation effects decrease as the total pressure and hence the relaxation rate of the system increase. Qualitatively, it can be seen that closer to the inhomogeneous broadening limit (low pressure) $S_{0,\gamma}$ is larger than $S_{0,\alpha}$, since only the Lorentzian component of the Voigt profile is fitted to obtain the former parameter. At the higher pressure limit, the relative sizes of the two parameters is inverted and the assumption that the system is homogeneously saturated becomes more adequate, making $S_{0,\gamma}$ more appropriate for quantifying saturation in this limit.

The saturation intensity determined using the relaxation rate constant of $4.5 \text{ s}^{-1} \text{ Torr}^{-1}$, at a pressure of 75 Torr and an absorption cross section of $\sigma_0 = 2.24 \times 10^{-18} \text{ cm}^2$, is $I_0^{\text{sat}} \approx 5.6 \text{ W cm}^{-2}$. Assuming collisional relaxation to be the only relaxation mechanism would result in an overestimation of S_0 by a factor of ≈ 45 , indicating that other contributions to the total relaxation rate play a significant role. With cavity mirrors with a radius of curvature of 0.5 m, the beam waist of the Gaussian mode in the cavity is $\sim 1.2 \text{ mm}$ in diameter, leading to a transit-time of about $5 \mu\text{s}$ and a saturation intensity $I_0^{\text{sat}} = 3.4 \text{ kW cm}^{-2}$. Since the beam diameter almost doubles at the mirrors, this transit-time relaxation mechanism becomes slower and yields a saturation intensity of $\sim 1 \text{ kW cm}^{-2}$. The total relaxation time can then be seen as a combination of the effects mentioned above, along with pressure induced velocity

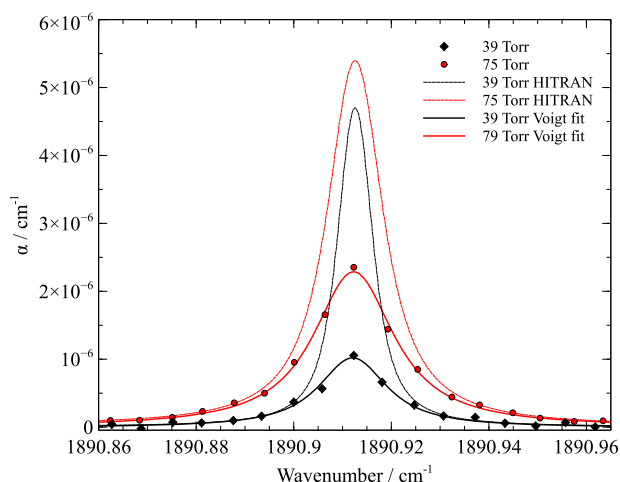


FIG. 3. OF-CEAS spectra of the $^2\Pi_{3/2}$ R(3.5) transition of NO taken at two different total pressures of 39 and 75 Torr with $p_{\text{NO}} = 0.94 \text{ ppmv}$, overlaid with simulations generated using the HITRAN database, for demonstrating the pressure dependent saturation of the absorption line shape. Both spectra were obtained with the TEM₁₀ transverse mode. Voigt fits to the experimental data are also shown.

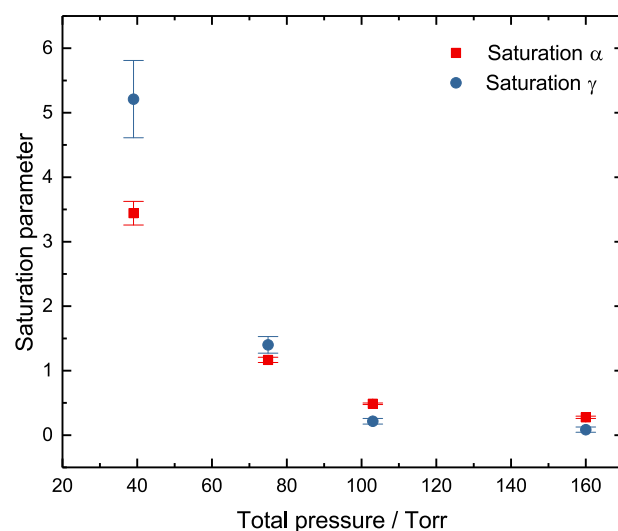


FIG. 4. Saturation parameters calculated using homogeneous widths and absorption coefficients for the NO $^2\Pi_{3/2}$ R(3.5) transition as a function of total pressure. All data were taken at constant intensity and using the TEM₁₀ mode.

changing collisions and rotational energy transfer within the upper vibrational state. The final parameter which influences the degree of saturation in our spectrometer is the transverse cavity mode (TEM) used. Aside from the change in intensity distribution within the cavity that comes with a higher TEM mode, the effective path length, and hence the finesse, will also be reduced due to increased diffraction losses. This effect was verified with the spectra of a species at known concentration that does not saturate under the same experimental conditions. Specifically, we chose 100% CO₂ (BOC) as it absorbs in the same spectral region as the NO $^2\Pi_{3/2}$ R(3.5) transition, but its transitions have considerably lower absorption cross sections; the $(1\ 1^1\ 0) \leftarrow (0\ 0^0\ 0)$ P(15) transition of $^{16}\text{O}^{12}\text{C}^{18}\text{O}$, the strongest in the spectrum shown in Fig. 5, has a cross section of $\sigma_0 = 2.3 \times 10^{-24}$ cm² which is $\approx 10^6$ times lower than the aforementioned NO transition. Saturating these transitions would require intensities on the order of MW cm⁻². The difference in the ratio of cavity transmission with absorber, T_a , to cavity transmission without absorber, T_0 , shown in Fig. 5, is a manifestation of effective path length reduction due to higher diffraction losses with the higher order mode, resulting in an apparent reduction of mirror reflectivity from ≈ 0.9998 to ≈ 0.9997 . It is therefore important to assess the degree of saturation in each individual case taking into consideration that the effective path length may also be altered, hence calibrating the spectrometer either with a non-saturable species of known concentration at the same experimental conditions or taking an empty-cavity CRDS measurement is vital.

Figure 6 compares the saturation effects in INFAMOS to those observed in OF-CEAS. These data were taken with

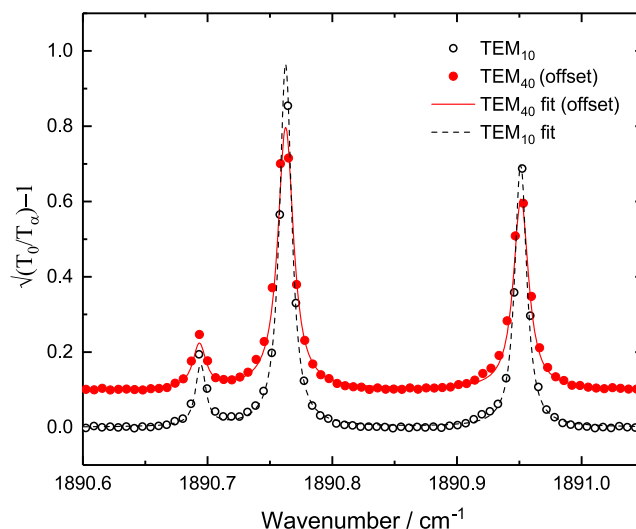


FIG. 5. OF-CEAS spectra of pure CO₂ observed with the TEM₁₀ and TEM₄₀ cavity modes at 41 Torr and 56 Torr total pressure, respectively. The spectrum acquired with the TEM₄₀ mode is offset by 0.1 for clarity.

samples of NO mixed in nitrogen with a volume fraction of 110 ppbv and 602 ppbv at 237 Torr and 42 Torr, respectively, and a magnetic field amplitude of 85 G. By overlaying the spectra taken at different pressures with simulations based on our model for unsaturated INFAMOS,²¹ a clear discrepancy is seen between the experimental data and the simulations in Fig. 6. This discrepancy can be qualitatively described as a change in the ratio between the amplitude of the signal at line centre (*a*) and the amplitude of the lobes (*b*)—a change in the *aspect ratio* of the signal. The centre:lobe amplitude ratio of

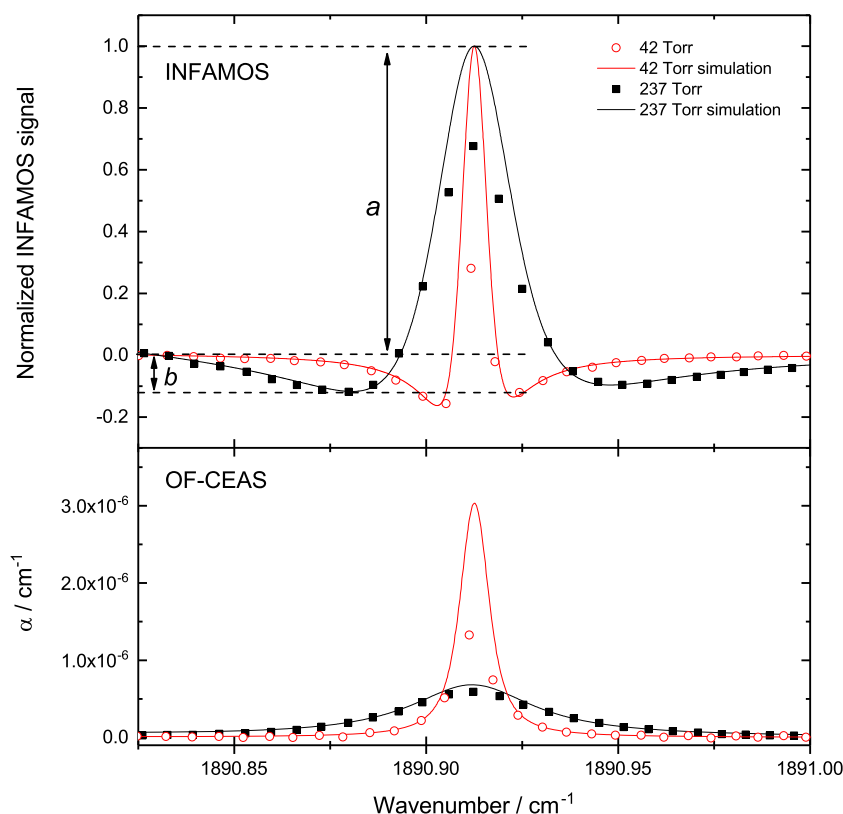


FIG. 6. Top panel: INFAMOS spectra of the NO $^2\Pi_{3/2}$ R(7/2) transition at 42 Torr and 237 Torr overlaid with simulations using an unsaturated line shape model for INFAMOS. Bottom panel: OF-CEAS spectra acquired simultaneously, overlaid with simulations of the unsaturated line shape using pressure broadening parameters and cross sections from HITRAN.

the simulated line shapes, represented in Fig. 6 as the ratio a/b , using the left lobe for all comparisons, increases from 6.7 at 42 Torr to 8 at 237 Torr. The measured spectra, however, underestimate this ratio by approximately a factor of 4 and a factor of 2, respectively, and approach the simulated values at higher pressures. The simultaneously acquired OF-CEAS spectra presented in the bottom panel of Fig. 6 show that the reduction in the absorption coefficient caused by saturation translates into a reduction in the aspect ratio of the INFAMOS signals.

To understand the line shape change caused by saturation, consider the dispersive line shapes presented in Fig. 7(a) for a LHCP wave. Optical pumping reduces the population of the lower states, $|J, M\rangle$, and increases the population of the upper states, $|J', M'\rangle$, leading to a reduced contribution from each sub-transition to the phase-shift (refractive index) experienced by a LHCP wave. These contributions are shown for two examples with $S_0 = 0$ and $S_0 = 5$. The inset shows the centre positions and relative absorption cross sections (or transition moments) of the 8 contributing sub-transitions associated with the R(3.5) transition. In Fig. 7(b), the Faraday rotation angle spectra and the total phase-shifts for a LHCP wave are shown for $S_0 = 0$ and $S_0 = 5$. The unsaturated line shape, $S_0 = 0$, is

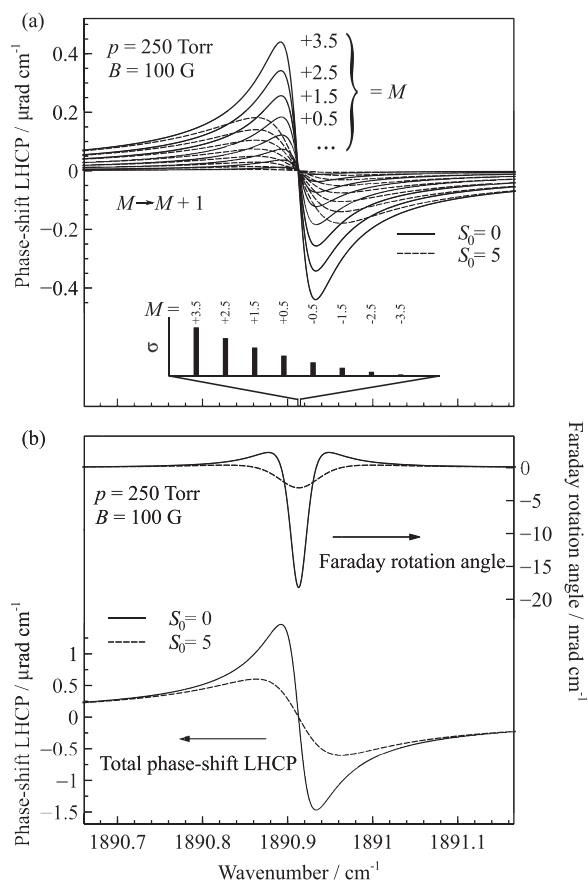


FIG. 7. (a) Phase-shifts induced by the 8 sub-transitions, $M \rightarrow M + 1$, $-3.5 \leq M \leq +3.5$, of the $^2\Pi_{3/2}$ R(3.5) transition for saturation parameter values of $S_0 = 0$ and $S_0 = 5$. For clarity, the other 8 sub-transitions, $M \rightarrow M - 1$, are not shown. Also shown are the relative absorption cross sections for each of the 8 sub-transitions. (b) Top: Faraday rotation angle for $S_0 = 0$ and $S_0 = 5$. Bottom: Total phase-shifts experienced by a LHCP wave ($M \rightarrow M + 1$) for $S_0 = 0$ and $S_0 = 5$. Conditions for (a) and (b): pressure, 250 Torr; magnetic field strength, 100 G.

well known, but the saturated one, $S_0 = 5$, is reduced at the line centre to $\sim 25\%$ of its unsaturated amplitude. Figure 8(a) illustrates this behaviour further by showing the evolution of the Faraday rotation spectrum as a function of the saturation parameter. The parameters used for the evaluation of the model [Eq. (17)] are given in Table I. It is clear that the INFAMOS line shape is strongly dependent upon the saturation parameter. Studies on saturation effects in NICE-OHMS^{18–20} have shown that the dispersive line shape function is virtually unaffected by the large intracavity irradiance in the limit of pure Doppler-broadening—in contrast to the absorptive line shape—but that with increasing pressures, saturation effects become more and more pronounced (see Fig. 1 in Ref. 19). Here, we limit ourselves to the homogeneously broadened limit for two reasons. The first one is that the FSR of the cavity is slightly larger than the Doppler-width of NO, meaning that a substantial number of data points across a line is only achieved with pressure broadened samples; we note however that interleaving techniques could be used if spectra were required to be measured with Doppler limited resolution. The second reason is that it affords simplifying assumptions for the modelling of the INFAMOS signal. In their theoretical work, Ma *et al.*¹⁹ assumed a two-level system, an assumption that was validated experimentally by the same group.¹⁸ In our case, however, the Zeeman effect splits the upper and lower levels into $2J' + 1$ and $2J + 1$ sub-levels, respectively. In the homogeneously broadened limit, we can readily make assumptions about the population distribution among these sub-levels (see Appendix B). Hence, our measurements are always far from the Doppler limit and it is the case that the dispersion signal (in the form of the INFAMOS line shape) shows considerable variation as a function of saturation parameter.

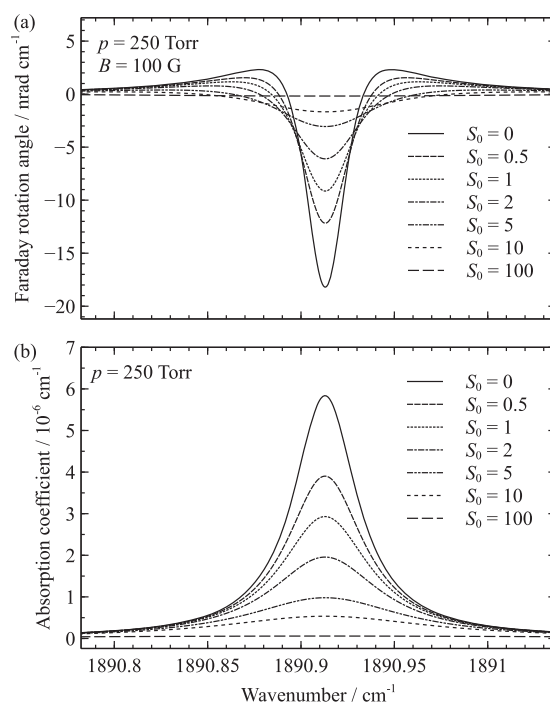


FIG. 8. (a) INFAMOS and (b) absorption coefficient line shapes as a function of the saturation parameter. Conditions: pressure: 250 Torr, magnetic field strength [for (a)]: 100 G.

TABLE I. Parameters used for the simulation of the phase-shifts in Fig. 7.

Parameter	Value	Unit	References
Angular momentum J	3.5 \rightarrow 4.5		39
g -factor g	0.187 012 \rightarrow 0.110 396		39
Zeeman splitting $\frac{\mu_B g}{hc}$	$8.731 \times 10^{-6} \rightarrow 5.154 \times 10^{-6}$	cm^{-1}/G	39
Molecular mass	4.9815×10^{-26}	kg	
Line strength \mathcal{S}	4.6454×10^{-20}	$\text{cm}^2 \text{cm}^{-1}$	40
Transition frequency ν_0	1890.913	cm^{-1}	40
Pressure-broadening parameter	8.13×10^{-5}	$\text{cm}^{-1}/\text{Torr}$	40
Doppler width (HWHM)	2.13×10^{-3}	cm^{-1}	
Lorentzian width (HWHM) γ	2.03×10^{-2}	cm^{-1}	
Pressure	250	Torr	
Temperature	298	K	
Magnetic field B	100	G	
Concentration	1	ppm	

The model for the saturated phase-shift [Eq. (17)] allows the Faraday rotation angle to be computed via Eq. (1) ($\phi^L = \phi_{+1}$, $\phi^R = \phi_{-1}$) with S_0 as a free parameter. Figure 9 compares the measured INFAMOS signal obtained at 237 Torr with a model for the saturated INFAMOS line shape with $S_0 = 0.3$. Here the INFAMOS signal has been converted into a calibrated Faraday rotation angle, using the electronic and optical responses of the lock-in amplifier and the polarizer/analyzer systems, respectively. Further details of this calibration are given in Appendix F. The model also takes into account the $^2\Pi_{1/2}$ doublet transition at $\sim 1890.7 \text{ cm}^{-1}$, which at 237 Torr gives a significant contribution to the refractive index in the spectral range of Fig. 9. There is reasonably good agreement between the simulation and experimental data, particularly in terms of the amplitudes and widths of the signals, giving confidence in the validity of the model. Nevertheless, there is a significant discrepancy towards the left side of the spectrum, for which a number of factors could be responsible. These are as follows: (1) Homogeneity of the magnetic field.

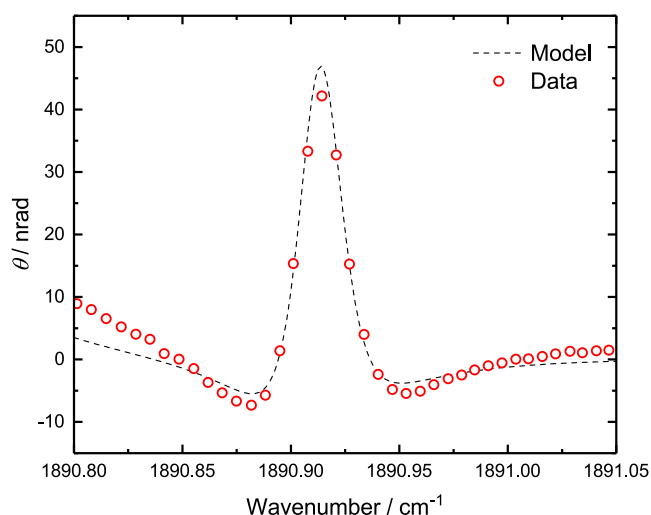


FIG. 9. INFAMOS spectrum obtained at 237 Torr and a magnetic field amplitude of 85 G overlaid with a simulation produced using the saturated INFAMOS model.

The on-axis longitudinal magnetic field of a solenoid with a radius much smaller than its length is relatively homogeneous within the solenoid but falls off to zero outside of it. The NO molecules thus experience a non-constant magnetic field, a fact that was not taken into account in the model. (2) The intensity (irradiance) of the laser beam is dependent on the position within the cavity. This leads to position-dependent rates of optical pumping and thus to a non-uniform saturation parameter. To some extent, this phenomenon is mitigated by the thermal motion of the molecules. (3) Even though we use Voigt line shapes, the model was derived in the limit of homogeneous broadening. Despite these limitations, we note that the best fit saturation parameter for the INFAMOS signal (computed with a least-squares procedure) is $S_0 = 0.3$; this is in good agreement with the same parameter derived from OF-CEAS data obtained under the same conditions. The saturation intensity of this NO transition under the selected experimental conditions is $I_0^{\text{sat}} = 1.5 \text{ kW cm}^{-2}$, corresponding to an excited state relaxation time of $30 \mu\text{s}$. This short upper state lifetime is consistent with a significant transit-time contribution to the molecular relaxation.

V. CONCLUSIONS

Intracavity peak intensities of $\sim 1 \text{ kW cm}^{-2}$ are readily achievable with moderately high finesse cavities in the mid-IR. Such intensities are capable of producing large changes in population when exciting a strong R-branch transition of NO, resulting in saturation making a significant contribution to the line shapes of both INFAMOS and OF-CEAS spectra. A model that uses a single saturation parameter to predict the dispersive line shape under a saturating field was developed, extending the range of experimental conditions under which INFAMOS can be applied and signals quantified, in this case to pressures $< 400 \text{ Torr}$, where saturation effects become significant. The saturation parameter of $S_0 = 0.3$ at 237 Torr extracted via this model is in good agreement with the saturation parameters extracted from OF-CEAS measurements and correspond to relaxation times of the order of $30 \mu\text{s}$ at this pressure.

ACKNOWLEDGMENTS

This work was funded by the Natural Environment Research Council (NERC) (No. NE/M016439/1).

APPENDIX A: LINE SHAPES

1. Homogeneous line shapes

When a transition is probed by monochromatic light, the dependence of the *absorption coefficient*, α , and of the *refractive index*, n , on the wavenumber, ν , is described by a pair of *line shape functions*. One can distinguish between two cases: (a) if all the molecules in the sample have the same line shape (e.g., due to collisional broadening), the transition is said to be *homogeneously broadened*; (b) if the line shape varies among the molecules in the sample (e.g., due to the Doppler effect), the transition is said to be *inhomogeneously broadened*. Assume a plane wave of the form

$$E(z, t) = \hat{E} \exp[-ik\tilde{n}z] \exp[2\pi i\nu ct] \quad (A1)$$

propagating through the gaseous sample, with \hat{E} being the polarization vector, $k = 2\pi\nu$ being the magnitude of the wave vector, and \tilde{n} being the complex refractive index. With a classical model (damped oscillating dipoles, see, for example, Chap. 3 in Ref. 38), it is possible to derive the forms of the real and imaginary part of the complex refractive index for a collection of identical molecules

$$n \doteq \Re[\tilde{n}] = 1 - \mathcal{X} \frac{1}{\pi} \frac{\nu - \nu_0}{(\nu - \nu_0)^2 + \gamma^2}, \quad (A2)$$

$$\kappa \doteq -\Im[\tilde{n}] = \mathcal{X} \frac{1}{\pi} \frac{\gamma}{(\nu - \nu_0)^2 + \gamma^2}, \quad (A3)$$

where γ is the Lorentzian width (HWHM), ν_0 is the transition (resonance) frequency, and \mathcal{X} (let us call it the transition strength) is a property of the transition under investigation which includes the transition moment and the population of the upper and lower states. By defining the *homogeneous line shape functions*

$$\mathcal{L}(\nu; \nu_0) = -\frac{1}{\pi} \frac{\nu - \nu_0}{(\nu - \nu_0)^2 + \gamma^2}, \quad (A4)$$

$$\mathcal{L}'(\nu; \nu_0) = \frac{1}{\pi} \frac{\gamma}{(\nu - \nu_0)^2 + \gamma^2}, \quad (A5)$$

we can write (A2) and (A3) more compactly as

$$n = 1 + \mathcal{X} \mathcal{L}'(\nu; \nu_0), \quad (A6)$$

$$\kappa = \mathcal{X} \mathcal{L}(\nu; \nu_0). \quad (A7)$$

The real part of \tilde{n} [(A6)] is just the ordinary refractive index, whereas the imaginary part, κ [(A7)], can be linked to the absorption coefficient through Beer-Lambert's law

$$|E(z, t)|^2 \sim I \exp[-2k\kappa z] \doteq I \exp[-\alpha z], \quad (A8)$$

yielding

$$\alpha = 4\pi\nu \mathcal{X} \mathcal{L}(\nu; \nu_0). \quad (A9)$$

Notice that since \mathcal{L} [(A5)] is area-normalized to unity, its peak amplitude is inversely proportional to the width

$$\mathcal{L}(\nu_0; \nu_0) = \frac{1}{\pi\gamma}. \quad (A10)$$

2. Inhomogeneous line shapes

If the molecules possess velocity v parallel to the probe beam, then the line shapes are frequency-shifted by the Doppler-shift

$$\nu_D = \nu_0 \frac{v}{c}. \quad (A11)$$

If $\mathcal{G}(\nu_D)d\nu_D$ indicates the fraction of molecules with Doppler-shift between ν_D and $\nu_D + d\nu_D$, where $\mathcal{G}(\nu_D)$ is the Maxwell-Boltzmann velocity distribution

$$\mathcal{G}(\nu_D)d\nu_D = \sqrt{\frac{1}{\pi}} \frac{\sqrt{\ln 2}}{\gamma_D} \exp\left[-\left(\frac{\sqrt{\ln 2}}{\gamma_D} \nu_D\right)^2\right] d\nu_D, \quad (A12)$$

then the refractive index and absorption coefficient become

$$n(\nu) = 1 + \mathcal{X} \int \mathcal{L}'(\nu; \nu_0 + \nu_D) \mathcal{G}(\nu_D) d\nu_D, \quad (A13)$$

$$\alpha(\nu) = 4\pi\nu \mathcal{X} \int \mathcal{L}(\nu; \nu_0 + \nu_D) \mathcal{G}(\nu_D) d\nu_D. \quad (A14)$$

By writing \mathcal{X} outside of the integral, we are implying that the transition strength of a molecule does not depend on its velocity; that is, we are assuming that no spectral hole burning (Bennett holes) occurs. This is not true at very low pressures where the population difference of a specific velocity group can be altered by strong optical pumping (e.g., Lamb dip spectroscopy). The integrals in (A13) and (A14) can be written with the scaled complementary error function w ⁴¹ as

$$\chi(\nu; \nu_0) \doteq -\frac{\sqrt{\ln 2}}{\gamma_D} \frac{1}{\sqrt{\pi}} \Im\left[w\left(\frac{\sqrt{\ln 2}}{\gamma_D}(\nu - \nu_0 + i\gamma)\right)\right] \quad (A15)$$

$$\eta(\nu; \nu_0) \doteq \frac{\sqrt{\ln 2}}{\gamma_D} \frac{1}{\sqrt{\pi}} \Re\left[w\left(\frac{\sqrt{\ln 2}}{\gamma_D}(\nu - \nu_0 + i\gamma)\right)\right], \quad (A16)$$

respectively, where γ_D is the Doppler-width (HWHM)

$$\gamma_D \doteq \nu_0 \sqrt{\frac{2k_B T \ln 2}{mc^2}}, \quad (A17)$$

with T being the temperature and m being the mass of the molecule. The absorptive line shape, η , is the well known *Voigt function*, and χ is its dispersive counterpart. The refractive index and absorption coefficient thus become

$$n(\nu) = 1 + \mathcal{X} \chi(\nu; \nu_0), \quad (A18)$$

$$\alpha(\nu) = 4\pi\nu \mathcal{X} \eta(\nu; \nu_0). \quad (A19)$$

Notice that since both \mathcal{L} and \mathcal{G} are normalized to unit area, so is η (since it is a convolution of \mathcal{L} and \mathcal{G}).

With a magnetic field present, the absorptive and dispersive line shapes of a transition $|J, M\rangle \rightarrow |J', M'\rangle$ ⁴² are Zeeman-shifted compared to the zero-field case and centred at

$$\nu_0^{MM'} = \nu_0 + (g'M' - gM) \frac{\mu_B B}{hc}, \quad (A20)$$

where g and g' are the g -factors of the lower and upper states, respectively. The refractive index and absorption coefficient then become weighted sums of contributions from each allowed transition

$$n(\nu) = 1 + \mathcal{R} \sum_{M,M'} \bar{w}^{MM'} \chi(\nu; \nu_0^{MM'}) \doteq 1 + \mathcal{R} \mathcal{M}'(\nu), \quad (\text{A21})$$

$$\alpha(\nu) = 4\pi\nu \mathcal{R} \sum_{M,M'} \bar{w}^{MM'} \eta(\nu; \nu_0^{MM'}) \doteq 4\pi\nu \mathcal{R} \mathcal{M}(\nu), \quad (\text{A22})$$

where $\bar{w}^{MM'}$ is the relative intensity of the transition $|J, M\rangle \rightarrow |J', M'\rangle$ and

$$\sum_{M,M'} \bar{w}^{MM'} = 1. \quad (\text{A23})$$

APPENDIX B: UNSATURATED ABSORPTION AND REFRACTIVE INDEX

The *line strength*, \mathcal{S} , for an electric dipole transition $|J\rangle \rightarrow |J'\rangle$ without any external magnetic field is defined in Ref. 43 as (in SI units)

$$\mathcal{S} \doteq \frac{2\pi^2\nu_0}{3hc\epsilon_0} \frac{\mathcal{N}_J}{\mathcal{N}} \left[1 - \frac{g_J}{g_{J'}} \frac{\mathcal{N}_{J'}}{\mathcal{N}_J} \right] \mathcal{R}, \quad (\text{B1})$$

where \mathcal{N}_J and $\mathcal{N}_{J'}$ are the population number densities in thermodynamic equilibrium (TDE) at $T = 298$ K

$$\mathcal{N}_J = \mathcal{N} g_J e^{-\frac{E_J}{k_B T}}, \quad (\text{B2})$$

$g_J, g_{J'}$ are the statistical weights, \mathcal{N} is the molecular number density, \mathcal{R} is the total dipole transition moment, and Q is the partition sum. The (unsaturated) absorption coefficient, α , in thermodynamic equilibrium (TDE) at the temperature T is then simply

$$\alpha(\nu) = \mathcal{N} \mathcal{S} \eta(\nu; \nu_0). \quad (\text{B3})$$

With a magnetic field present, the states $|J\rangle$ split into sub-states $|J, M\rangle$. The observed absorption at the frequency ν is then the sum of the contributions from all sub-transitions $|J, M\rangle \rightarrow |J', M'\rangle$

$$\alpha_q(\nu) = \mathcal{N} \mathcal{S} \sum_{M,M'} w_q^{MM'} \eta(\nu; \nu_0^{MM'}). \quad (\text{B4})$$

How much each sub-transition contributes to the total absorption depends on two factors: (i) the population of the upper and lower state; (ii) the transition moment for the specific sub-transition. For circularly polarized light propagating along the field axis, the transition moments for the sub-transition $|J, M\rangle \rightarrow |J', M'\rangle$ are of the form $\langle J', M' | \mu_q | J, M \rangle$, where $q = +1$ for a LHCP wave, $q = -1$ for a RHCP wave, and μ_q ($q = \pm 1$) are the spherical components of the dipole moment operator. Since the selection rules for μ_{+1} and μ_{-1} are different, we obtain two different absorption values depending on the polarization of the wave. Assuming all sub-states $|J, M\rangle$ with the same J quantum number to be equally populated

$$\mathcal{N}_{JM} = \frac{\mathcal{N}_J}{g_J}, \quad \forall M, \quad (\text{B5})$$

and with the Wigner-Eckart theorem, one can show³⁵ that the weights, $w_q^{MM'}$, for a rovibrational transition take on the form

$$w_q^{MM'} = 3 \begin{pmatrix} J' & 1 & J \\ -M' & q & M \end{pmatrix}^2, \quad (\text{B6})$$

where the term in parentheses is the Wigner 3j symbol. The sum in (B4) is then of the form (A22). We thus have the absorptive line shape function, \mathcal{M}

$$\mathcal{M}_q(\nu) = 3 \sum_{M,M'} \begin{pmatrix} J' & 1 & J \\ -M' & q & M \end{pmatrix}^2 \eta(\nu; \nu_0^{MM'}), \quad (\text{B7})$$

and the dispersive line shape function, \mathcal{M}' ,

$$\mathcal{M}'_q(\nu) = 3 \sum_{M,M'} \begin{pmatrix} J' & 1 & J \\ -M' & q & M \end{pmatrix}^2 \chi(\nu; \nu_0^{MM'}). \quad (\text{B8})$$

APPENDIX C: SATURATED ABSORPTION AND REFRACTIVE INDEX

The above is valid if the populations of the states are in thermodynamic equilibrium. This is obviously not the case in the regime of optical saturation. We introduce the saturated populations

$$N_J(\nu) = \mathcal{N}_J f_J(\nu), \quad (\text{C1})$$

and we still assume that all the sub-states $|J, M\rangle$ are equally populated. This implies the assumption that there are very fast relaxation processes between states with the same x and J quantum numbers. The factor $f_J(\nu)$ accounts for the depletion (or population) of the state and is unity in TDE. To obtain the saturated absorption and refractive index, we must substitute the TDE populations, \mathcal{N}_J , in (B1) with the saturated populations, N_J [(C1)]. Hence, we must carry out the substitution

$$\mathcal{S} \rightarrow \mathcal{S} \frac{N_J(\nu) \left[1 - \frac{g_J}{g_{J'}} \frac{N_{J'}(\nu)}{N_J(\nu)} \right]}{\mathcal{N}_J \left[1 - \frac{g_J}{g_{J'}} \frac{\mathcal{N}_{J'}}{\mathcal{N}_J} \right]}. \quad (\text{C2})$$

With $E_{J'} - E_J \approx 1900 \text{ cm}^{-1}$ and $k_B T \approx 200 \text{ cm}^{-1}$, the fractional term in the brackets in the denominator of (C2) can be neglected [see (B2)], and we obtain with (C1)

$$\mathcal{S} \rightarrow \mathcal{S} \cdot \left[f_J(\nu) - \frac{g_J}{g_{J'}} \frac{\mathcal{N}_{J'}}{\mathcal{N}_J} f_{J'}(\nu) \right]. \quad (\text{C3})$$

With the definition

$$p(\nu) \doteq \left[f_J(\nu) - \frac{g_J}{g_{J'}} \frac{\mathcal{N}_{J'}}{\mathcal{N}_J} f_{J'}(\nu) \right], \quad (\text{C4})$$

and after carrying out the substitution (C3) in (B4), we have with (B7)

$$\alpha_q(\nu) = \mathcal{N} \mathcal{S} p(\nu) \mathcal{M}_q(\nu). \quad (\text{C5})$$

Comparison of (C5) with (A22) yields

$$\mathcal{R} = \frac{1}{4\pi\nu} \mathcal{N} \mathcal{S} p, \quad (\text{C6})$$

and for the refractive index, we have from (A21) and (C6)

$$n_q(\nu) = 1 + \frac{1}{4\pi\nu} \mathcal{N} \mathcal{S} p(\nu) \mathcal{M}'_q(\nu). \quad (\text{C7})$$

APPENDIX D: POPULATION DIFFERENCE

Assuming a 2-level system, the rate equation for $N_J = \mathcal{N}_J f_J$ is

$$\mathcal{N}_J \dot{f}_J = -\mathcal{B} I \mathcal{N}_J p \mathcal{M}_q + \mathcal{A} \mathcal{N}_J f_{J'}, \quad (\text{D1})$$

where \mathcal{A} and \mathcal{B} are the Einstein coefficients (in the appropriate units) and I is the irradiance (power per unit area) of the wave. We further assume that the total number of molecules in both upper and lower states with optical pumping is the same as without pumping in TDE

$$N_J + N_{J'} = \mathcal{N}_J + \mathcal{N}_{J'}. \quad (\text{D2})$$

At room temperature, $k_B T \approx 200 \text{ cm}^{-1}$ and for $E_{J'} - E_J \approx 1900 \text{ cm}^{-1}$, we have $\mathcal{N}_{J'} \ll \mathcal{N}_J$. Then from (D2) with (B2) follows

$$f_{J'} \approx (1 - f_J) \frac{\mathcal{N}_J}{\mathcal{N}_{J'}}. \quad (\text{D3})$$

The steady-state ($\dot{f}_J = 0$) solution of (D1) is

$$f_J(\nu) = \frac{1 + I \frac{\mathcal{B}}{\mathcal{A}} \frac{g_J}{g_{J'}} \mathcal{M}_q(\nu)}{1 + I \frac{\mathcal{B}}{\mathcal{A}} \left(1 + \frac{g_J}{g_{J'}}\right) \mathcal{M}_q(\nu)}, \quad (\text{D4})$$

and with (D3), we find for p [(C4)]

$$p_q(\nu) = \frac{1}{1 + I \frac{\mathcal{B}}{\mathcal{A}} \left(1 + \frac{g_J}{g_{J'}}\right) \mathcal{M}_q(\nu)}. \quad (\text{D5})$$

By defining the *saturation intensity* (actually, irradiance), I_q^{sat} ,

$$I_q^{\text{sat}}(\nu) \doteq \frac{\mathcal{A}}{\mathcal{B} \left(1 + \frac{g_J}{g_{J'}}\right) \mathcal{M}_q(\nu)}, \quad (\text{D6})$$

and the *saturation parameter*

$$\begin{aligned} S_q(\nu) &\doteq \frac{I}{I_q^{\text{sat}}(\nu)} \\ &= I \frac{\mathcal{B}}{\mathcal{A}} \left(1 + \frac{g_J}{g_{J'}}\right) \mathcal{M}_q(\nu) \\ &= \pi \gamma S_0 \mathcal{M}_q(\nu), \end{aligned} \quad (\text{D7})$$

with

$$S_0 = \frac{I}{\pi \gamma} \frac{\mathcal{B}}{\mathcal{A}} \left(1 + \frac{g_J}{g_{J'}}\right), \quad (\text{D8})$$

we have for p_q [(D5)]

$$p_q(\nu) = \frac{1}{1 + S_q(\nu)}. \quad (\text{D9})$$

Remark: In the high-pressure, zero-field case ($\mathcal{M} = \mathcal{L}$), the population difference at the transition centre, ν_0 , is with (A10)

$$p = \frac{1}{1 + S_0}, \quad (\text{D10})$$

and the saturation intensity at ν_0 , I_0^{sat} , is with (D6)

$$I_0^{\text{sat}} = \pi \gamma \frac{\mathcal{A}}{\mathcal{B} \left(1 + \frac{g_J}{g_{J'}}\right)}. \quad (\text{D11})$$

The Einstein coefficient, \mathcal{A} , is inversely proportional to the upper state lifetime, $\tau^{-1} \doteq \mathcal{A}$, whereas $\mathcal{B} \sim \mathcal{S}$ is proportional

to the line strength. In the high-pressure limit considered here, the absorption cross section at the centre of the transition is $\sigma_0 \sim \mathcal{B}/(\pi \gamma)$ and we have

$$I_0^{\text{sat}} \sim \frac{1}{\sigma_0 \tau}. \quad (\text{D12})$$

APPENDIX E: SATURATED INFAMOS LINE SHAPE: SUMMARY

Combining (D9) and (D7) with (C7) and (C5), we have for the saturated refractive index and absorption coefficient

$$n_q(\nu) = 1 + \frac{1}{4\pi\nu} \frac{\mathcal{N} \mathcal{S} \mathcal{M}'_q(\nu)}{1 + \pi \gamma S_0 \mathcal{M}_q(\nu)}, \quad (\text{E1})$$

$$\alpha_q(\nu) = \frac{\mathcal{N} \mathcal{S} \mathcal{M}_q(\nu)}{1 + \pi \gamma S_0 \mathcal{M}_q(\nu)}. \quad (\text{E2})$$

The total phase-shift, $\phi_q = 2\pi \nu n_q(\nu) L$, experienced by a LHCP ($q = +1$) or RHCP ($q = -1$) wave is then

$$\phi_q(\nu) = 2\pi \nu L + \frac{\mathcal{N} \mathcal{S} L}{2} \frac{\mathcal{M}'_q(\nu)}{1 + \pi \gamma S_0 \mathcal{M}_q(\nu)}, \quad (\text{E3})$$

where L is the interaction length.

APPENDIX F: CALIBRATION OF INFAMOS DATA

The time-dependence of the Faraday rotation angle is approximately given by

$$\theta(t) = \frac{2\mathcal{F}}{\pi} \theta_0 \sin(\Omega t), \quad (\text{F1})$$

where $2\mathcal{F}/\pi = 4000$ is the cavity enhancement factor (\mathcal{F} : cavity finesse), θ_0 is the single-pass Faraday rotation angle when the field is at its maximum value, and Ω is the magnetic field modulation frequency. The photodetector output voltage (i.e., the lock-in *input* voltage), $u(t)$, which is proportional to the optical power transmitted through the analyzer, is given by

$$u(t) = u_0 \sin^2(\beta + \theta(t)) \approx \text{const} + \frac{4\mathcal{F}\beta\theta_0 u_0}{\pi} \sin(\Omega t), \quad (\text{F2})$$

where u_0 is the photodetector voltage without the analyzer present, β is the uncrossing angle, and we have assumed $\beta \ll 1$ and $\theta(t) \ll 1$. The rms amplitude ($1/\sqrt{2}$ of zero-to-peak amplitude) of the first harmonic of the signal is then

$$u_1 = \frac{1}{\sqrt{2}} \frac{4\mathcal{F}\beta\theta_0 u_0}{\pi}. \quad (\text{F3})$$

The lock-in *output* voltage is simply $U_1 = G u_1$, where G is the gain of the lock-in amplifier. For the data in Fig. 9, $u_0 \approx 0.52 \text{ V}$, $\beta = 35 \text{ mrad}$, $G = 5 \times 10^4$, and we find

$$\frac{\theta_0}{U_1} = \frac{1}{\frac{2\mathcal{F}}{\pi} \sqrt{2} G \beta u_0} \approx 2 \times 10^{-7} \text{ rad V}^{-1}. \quad (\text{F4})$$

¹J. Remillard, D. Uy, W. Weber, F. Capasso, C. Gmachl, A. Hutchinson, D. Sivco, J. Baillargeon, and A. Cho, *Opt. Express* **7**, 243 (2000).

²A. Castrillo, E. De Tommasi, L. Gianfrani, L. Sirigu, and J. Faist, *Opt. Lett.* **31**, 3040 (2006).

³N. Mukherjee and C. K. N. Patel, *Chem. Phys. Lett.* **462**, 10 (2008).

⁴T. W. Hänsch and B. Couillaud, *Opt. Commun.* **35**, 441 (1980).

- ⁵A. Arie, S. Schiller, E. K. Gustafson, and R. L. Byer, *Opt. Lett.* **17**, 1204 (1992).
- ⁶S. Borri, S. Bartalini, I. Galli, P. Cancio, G. Giusfredi, D. Mazzotti, A. Castrillo, L. Gianfrani, and P. De Natale, *Opt. Express* **16**, 11637 (2008).
- ⁷Y. H. Lien, D. K. Liu, and J. T. Shy, *Appl. Phys. B: Lasers Opt.* **96**, 111 (2009).
- ⁸N. Mukherjee, R. Go, and C. K. N. Patel, *Appl. Phys. Lett.* **92**, 111116 (2008).
- ⁹J. M. R. Kirkbride, S. K. Causier, E. A. McCormack, D. Weidmann, and G. A. D. Ritchie, *Phys. Chem. Chem. Phys.: PCCP* **15**, 2684 (2013).
- ¹⁰F. Moreno, J. M. Alvarez, J. C. Amaré, and E. Bernabeu, *J. Appl. Phys.* **56**, 1939 (1984).
- ¹¹T. W. Hänsch, I. S. Shahin, and A. L. Schawlow, *Phys. Rev. Lett.* **27**, 707 (1971).
- ¹²M. S. Feld, M. M. Burns, T. U. Kihl, P. G. Pappas, and D. E. Murnick, *Opt. Lett.* **5**, 3 (1980).
- ¹³K. B. MacAdam, A. Steinbach, and C. Wieman, *Am. J. Phys.* **60**, 1098 (1992).
- ¹⁴D. Lisak and J. T. Hodges, *Appl. Phys. B: Lasers Opt.* **88**, 317 (2007).
- ¹⁵G. Giusfredi, S. Bartalini, S. Borri, P. Cancio, I. Galli, D. Mazzotti, and P. De Natale, *Phys. Rev. Lett.* **104**, 110801 (2010).
- ¹⁶I. Galli, S. Bartalini, R. Ballerini, M. Barucci, P. Cancio, M. De Pas, G. Giusfredi, D. Mazzotti, N. Akikusa, and P. De Natale, *Optica* **3**, 385 (2016).
- ¹⁷I. Ventrillard, P. Gorroategi-Carbajo, and D. Romanini, *Appl. Phys. B: Lasers Opt.* **123**, 1 (2017).
- ¹⁸A. Foltynowicz, W. Ma, F. M. Schmidt, and O. Axner, *J. Opt. Soc. Am. B* **25**, 1156 (2008).
- ¹⁹W. Ma, A. Foltynowicz, and O. Axner, *J. Opt. Soc. Am. B* **25**, 1144 (2008).
- ²⁰O. Axner, W. Ma, and A. Foltynowicz, *J. Opt. Soc. Am. B* **25**, 1166 (2008).
- ²¹M. Gianella, T. H. Pinto, X. Wu, and G. A. D. Ritchie, *J. Chem. Phys.* **147**, 054201 (2017).
- ²²R. Lewicki, J. H. Doty, R. F. Curl, F. K. Tittel, and G. Wysocki, *Proc. Natl. Acad. Sci. U. S. A.* **106**, 12587 (2009).
- ²³P. Kluczynski, S. Lundqvist, J. Westberg, and O. Axner, *Appl. Phys. B: Lasers Opt.* **103**, 451 (2011).
- ²⁴B. Brumfield, W. Sun, Y. Wang, Y. Ju, and G. Wysocki, *Opt. Lett.* **39**, 1783 (2014).
- ²⁵J. Westberg, B. Siller, M. Beels, H. Waechter, and G. Wysocki, *Conf. Lasers Electro-Opt.* **3**, AM1J.3 (2016).
- ²⁶J. Morville, S. Kass, M. Chenevier, and D. Romanini, *Appl. Phys. B: Lasers Opt.* **80**, 1027 (2005).
- ²⁷D. Romanini, M. Chenevier, S. Kass, M. Schmidt, C. Valant, M. Ramonet, J. Lopez, and H. J. Jost, *Appl. Phys. B: Lasers Opt.* **83**, 659 (2006).
- ²⁸S. G. Baran, G. Hancock, R. Peverall, G. A. D. Ritchie, and N. J. van Leeuwen, *Analyst* **134**, 243 (2009).
- ²⁹M. Gianella, S. Reuter, A. L. Aguila, G. A. D. Ritchie, and J.-P. H. van Helden, *New J. Phys.* **18**, 113027 (2016).
- ³⁰D. Miyakoshi, M. Aoyama, T. Tohei, A. Minoh, and M. Tsukakoshi, *Jpn. J. Appl. Phys., Part 1* **36**, 7379 (1997).
- ³¹I. O. G. Davies, P. E. G. Baird, and J. L. Nicol, *J. Phys. B: At., Mol. Phys.* **20**, 5371 (1999).
- ³²J. D. Jackson, *Classical Electrodynamics*, 3rd ed. (Wiley, New York, 1998).
- ³³C.-Y. Chang and J.-T. Shy, *Appl. Opt.* **54**, 8526 (2015).
- ³⁴P. Pokrowsky, W. Zapka, F. Chu, and G. Bjorklund, *Opt. Commun.* **44**, 175 (1983).
- ³⁵J. Westberg, L. Lathdavong, C. M. Dion, J. Shao, P. Kluczynski, S. Lundqvist, and O. Axner, *J. Quant. Spectrosc. Radiat. Transfer* **111**, 2415 (2010).
- ³⁶L. Doyennette and M. Margottin-Maclou, *J. Chem. Phys.* **84**, 6668 (1986).
- ³⁷K. M. Manfred, L. Ciaffoni, and G. A. D. Ritchie, *Appl. Phys. B* **120**, 329 (2015).
- ³⁸W. Demtröder, *Laser Spectroscopy: Basic Concepts and Instrumentation*, 3rd ed. (Springer-Verlag, Berlin, Heidelberg, 2003).
- ³⁹K. Wu, L. Liu, Z. Chen, X. Cheng, Y. Yang, and F. Li, *J. Phys. B: At., Mol. Opt. Phys.* **50**, 035401 (2017).
- ⁴⁰L. S. Rothman, I. E. Gordon, Y. Babikov, A. Barbe, D. Chris Benner, P. F. Bernath, M. Birk, L. Bizzocchi, V. Boudon, L. R. Brown, A. Campargue, K. Chance, E. A. Cohen, L. H. Coudert, V. M. Devi, B. J. Drouin, A. Fayt, J. M. Flaud, R. R. Gamache, J. J. Harrison, J. M. Hartmann, C. Hill, J. T. Hodges, D. Jacquemart, A. Jolly, J. Lamouroux, R. J. Le Roy, G. Li, D. A. Long, O. M. Lyulin, C. J. Mackie, S. T. Massie, S. Mikhailenko, H. S. P. Müller, O. V. Naumenko, A. V. Nikitin, J. Orphal, V. Perevalov, A. Perrin, E. R. Polovtseva, C. Richard, M. A. H. Smith, E. Starikova, K. Sung, S. Tashkun, J. Tennyson, G. C. Toon, V. G. Tyuterev, and G. Wagner, *J. Quant. Spectrosc. Radiat. Transfer* **130**, 4 (2013).
- ⁴¹M. Abramowitz, I. A. Stegun, and D. Miller, *Handbook of Mathematical Functions with Formulas, Graphs and Mathematical Tables*, Volume 55 of National Bureau of Standards Applied Mathematics Series (United States Department of Commerce, National Bureau of Standards, 1965).
- ⁴² J is the angular momentum, and M is the projection of the angular momentum on the axis of the magnetic field. The remaining quantum numbers (e.g., vibrational state) are omitted for clarity.
- ⁴³L. Rothman, C. Rinsland, A. Goldman, S. Massie, D. Edwards, J.-M. Flaud, A. Perrin, C. Camy-Peyret, V. Dana, J.-Y. Mandin, J. Schroeder, A. McCann, R. Gamache, R. Wattson, K. Yoshino, K. Chance, K. Jucks, L. Brown, V. Nemtchinov, and P. Varanasi, *J. Quant. Spectrosc. Radiat. Transfer* **60**, 665 (1998).